A pore-scale investigation of the effect of nanoparticle injection on properties of sandy porous media

Journal of Contaminant Hydrology 253 (2023) 104126

Contents lists available at ScienceDirect

Journal of Contaminant Hydrology

journal homepage: www.elsevier.com/locate/jconhyd

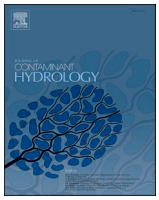

A pore-scale investigation of the effect of nanoparticle injection on properties of sandy porous media

Raoul Djou Fopa [a,*], Carlo Bianco [b], Nathaly Lopes Archilha [c], Anderson Camargo Moreira [d], Tannaz Pak [a]

[a] School of Computing, Engineering & Digital Technologies, Teesside University, United Kingdom
[b] Department of Environment, Land, and Infrastructure Engineering, Politecnico di Torino, Italy
[c] Brazilian Synchrotron Light Laboratory, Brazilian Canter for Research in Energy and Materials, Brazil
[d] LMPT Laboratory, Mechanical Engineering Department, Federal University of Santa Catarina, Brazil

ARTICLE INFO

Keywords:
Nanoparticles
Porous media
Nanoremediation
Pore network modelling
X-ray computed microtomography

ABSTRACT

Nanoremediation is a new groundwater remediation technology in which nanoparticles (NPs) are injected into the sub-surface to promote in-situ degradation of aquifer contaminants. Although nanoremediation is an effective process to eliminate contaminants in-situ, its success relies on sufficiently mobile NPs that can reach the contaminated zones and remain there to facilitate chemical degradation of contaminants. Therefore, understanding the main parameters that control the mobility and retention of NPs in saturated porous media is a key component of designing a successful nanoremediation process.

This work presents the outcome of a pore-scale study of nZVI NP (zero-valent iron) transport in sandy porous media using the non-destructive 3D imaging technique, X-ray computed micro-tomography (X-ray micro-CT). We investigate the effect of grain size (fine, coarse, carbonate and mixed sand) and composition (carbonate vs sand grains) on the mobility and retention of NPs in sand columns. To achieve this, we used four columns packed with grains of different sizes and compositions. The main contribution of this work is, therefore, to understand the effect of NP injection on the structural and geometric properties of sandy porous media and to identify the main pore-scale mechanisms controlling NP transport and entrapment.

Our experiment shows that the pore geometries change because of NP injection. Pore clogging is evidenced through pore size and throat size distribution displaying a shift to the left with a noticeable reduction in pore connectivity in all the columns. The porosity and permeability of the columns studied display significant reduction as result of the NP injection.

1. Introduction

Nanoparticles (NPs) are used in a wide range of applications including electronics, energy, biomedicine, textile, and the environment. They exhibit special physical and chemical properties due to their small size (1-100) nm (Suryanarayana et al., 1992). Importantly, NPs are shown to impact fluid flow in porous media that plays a key role in applications such as soil and groundwater remediation (Pak et al., 2019), geothermal energy (Zhang et al., 2020), and enhanced oil recovery (EOR), see the following review articles (Olayiwola and Dejam, 2019) and (Dordzie and Dejam, 2021). Added to this is the advancement in manufacturing technologies enabling cost effective production of NPs at large scale (Yu et al., 2010).

Nanoremediation is used to achieve in-situ degradation of aquifer contaminants effectively using reactive nanoparticles such as nZVI. To achieve this, nZVI is injected into the contaminated plume within the subsurface to promote the sorption, precipitation, and degradation of both organic and inorganic contaminants. The first field application of this technique was in 2001 for soil and groundwater treatment (Li et al., 2006). Extensive research is in progress to minimise the economic and environmental risks of nanoremediation (Karn et al., 2009). Detailed characterisation of complex porous media is important for a wide range of engineering and environmental applications such as environmental remediation, carbon capture and storage, and hydrocarbon recovery from subsurface.

2D and 3D images have been used to study porous media

* Corresponding author.
E-mail address: r.djoufopa@tees.ac.uk (R.D. Fopa).

https://doi.org/10.1016/j.jconhyd.2022.104126
Received 27 August 2022; Received in revised form 19 December 2022; Accepted 21 December 2022
Available online 23 December 2022

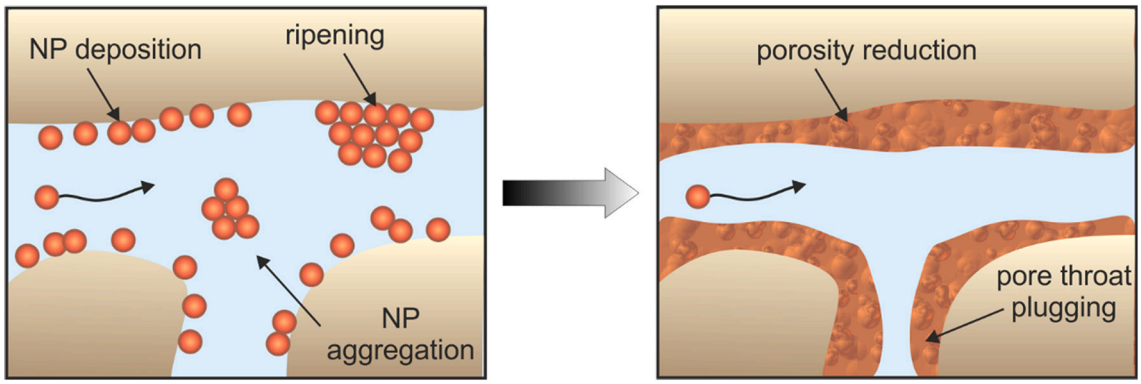

Fig. 1. NP mobility and retention mechanisms in porous media.

characteristics (e.g., pore volume and pore connectivity) as well as their single and multiphase fluid transport properties (Chen et al., 2015; Hidajat et al., 2002; Wildenschild and Sheppard, 2013; Pak et al., 2016). Fluid transport in porous media is a function of a range of key properties including porosity, permeability, pore connectivity, pore geometry, and pore size distribution (Al-Raoush and Willson, 2005). Pore- scale modelling is a tool used to simulate flow and NP transport at the pore and Darcy scale (Raoof et al., 2010; Sanematsu et al., 2019; Seetha et al., 2017). A useful approach to study pore-scale processes is to represent the pore system with a pore network which is a network of interconnected pores and pore throats (Baychev et al., 2019; Xiong et al., 2016). To achieve this, a 3D image of the porous media is required. This

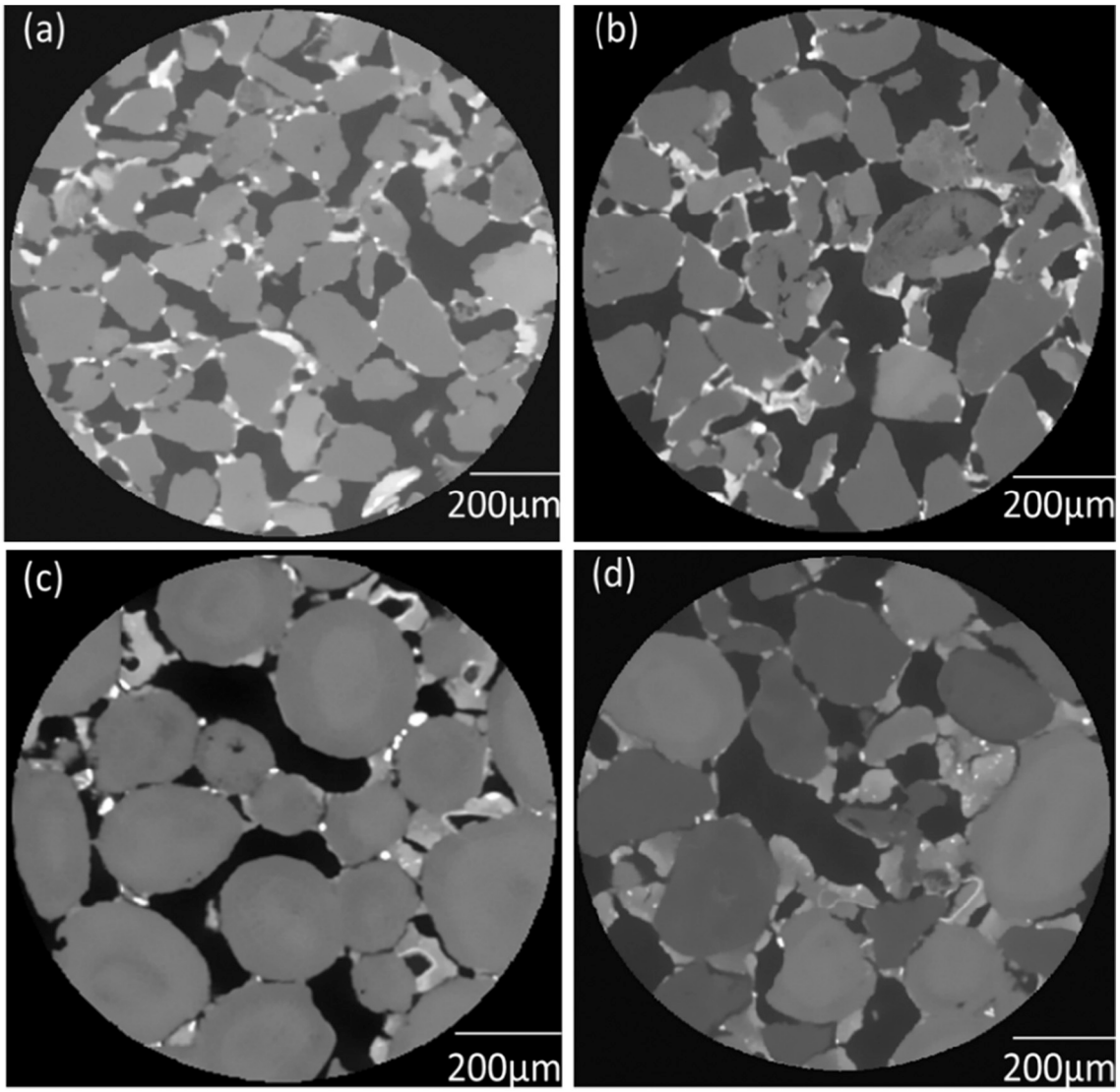

Fig. 2. 2D cross sections of 3D µCT images of different samples after nZVI injection. Fine sand (a); coarse sand (b); Carbonate (c) and the mixed sample (d).

image can be (i) directly obtained using X-ray computed micro-tomography imaging (Pak et al., 2016) or (ii) through 3D reconstruction based on information extracted from 2D images (Wu et al., 2006). Some complex pore systems require information extracted from more than one length-scale and combined in a meaningful way to achieve a representative pore network model (PNM), see (Pak et al., 2016).

PNM is a simple representation of the pore system using pore bodies and pore throats. In simpler PNMs, the pore shapes are commonly spherical while more advanced PNMs can also accommodate pores with other shapes mainly with the aim of capturing pore angularity and hence pore occupancy with more than one phase (Ryazanov et al., 2009). In a PNM, the coordination number is defined as the number of pore throats connected to a given pore (Lindquist et al., 2000). Coordination number is therefore a measure of the degree of connectivity of the network elements (pores and pore throats). The pore throat size (width) controls the effective hydraulic radius of the porous media mainly affecting its permeability.

Advances in the X-ray computed micro tomography imaging (X-ray micro-CT) technique has enabled the characterisation of porous media directly or through PNMs in a non-destructive way (Madonna et al., 2013; Sharqawy, 2016). Study of 3D images (or 4D in case of imaging a process with time) captured with the X-ray micro-CT technique has provided new insights into the key pore-scale mechanisms that control the flow. Samples commonly studied are sandstones, carbonates, coal, and shales. Pore-scale imaging and modelling is a field of research with significant growth in the past decade that aims at correlating the key macroscopic properties of porous media with its micro-scale characteristics. For example, (Madonna et al., 2013) quantitatively analysed the porous media characteristics for a range of carbonate and sandstone rocks using high resolution X-ray micro-CT imaging conducted at a synchrotron facility. Such imaging studies provide data (porosity, pore size distribution, pore connectivity, etc.) that can be used to calculate transport and mechanical properties of porous media as well e.g., electrical conductivity.

The nanoremediation process involves in-situ reaction between the injected NPs and the groundwater contaminants. In a field application, NP should be transported for long distances (in order of meters) for a successful nanoremediation process (Mohammadian et al., 2021). Researchers have been working on the different factors and processes that control the interaction of NP and the porous media (Beryani et al., 2020; Bianco et al., 2017). Since this interaction is a micro-scale process occurring within the pore space of aquifers, X-ray micro-CT technique can provide new insights into the dynamics of the nanoremediation process. To our knowledge the only studies published on this subject Pak et al., 2020 (the previous work of co-authors of this work) and Schiefler et al. (2022). While Pak et al. (2020) discuss the main pore-scale mechanisms that contribute to nanoremediation at the pore-scale (gas formation and flow, direct degradation at interface), their study does not discuss the mobility of nZVI nanoparticles within porous media which is a well-known challenge faced in field application of nanoremediation. Schiefler et al. (2022) is the first work focused on NP transport, studied at the pore scale, using micro-CT imaging. (Schiefler et al., 2022) shows that non-destructive micro-CT imaging can provide novel insights into nZVI mobility and entrapment within porous media and discuss the key pore-scale mechanisms contributing to the particle entrapment (straining and ripening). Building on the findings of this recently published study, our work focuses on applying a different approach, i.e., pore-network modelling to study the effect of nZVI injection on (i) pore-space geometry, (ii) pore-space connectivity, (iii) storage capacity (porosity), and (iv) flow properties (permeability) of sandy porous media. In practice, NP mobility in porous media is also controlled by the stability of NP suspension that can result in particle aggregation and deposition within pores (Mondino et al., 2020; Pak et al., 2018; Tiraferri et al., 2017) which is another challenge in field application of nanoremediation. Fig. 1 shows the main pore-scale mechanisms that control NP transport and retention within porous media.

2. Materials and methods

We performed experiments to investigate the impact of grain size and composition on nZVI mobility and retention in groundwater systems. These experiments allowed us to investigate the change in the structural and the geometric properties of sandy porous media as a result of NP injection. We studied four columns packed with fine sand, coarse sand, carbonate, and mix sand (comprising sand and carbonate grains). Fig. 2 shows example X-ray micro-CT slices for these four columns. These images were captured after the nZVI injection was completed so the nZVI phase is also visible in these slices. The columns were initially water saturated; subsequently the nZVI suspension was injected followed by a post water flush to remove the mobile nanoparticles. 3D volumetric images were captured at this point using X-ray micro-CT technique. All tomographic data presented here are at 4.52 μm resolution. Obtaining 3D images allows 3D visualisation as well as quantification of the different phases present within the sample. The image analysis and simulation were carried out using the freely available software ImageJ and the commercially available software Avizo.

2.1. Image processing and analysis workflow

The image analysis flowchart is shown in Fig. 3. Image processing includes noise filtering, segmentation, and analysis to study the transport and mobility of nZVI in the different samples. We calculated the flow properties (porosity and permeability) to compare the structural and geometric properties of the samples before and after nZVI injection. Fig. 3 shows that image acquisition and reconstruction steps were followed by image filtering using the non-local means filter (Buades et al., 2005) to remove the measurement noise while maintaining the image sharpness by preserving the phase boundaries.

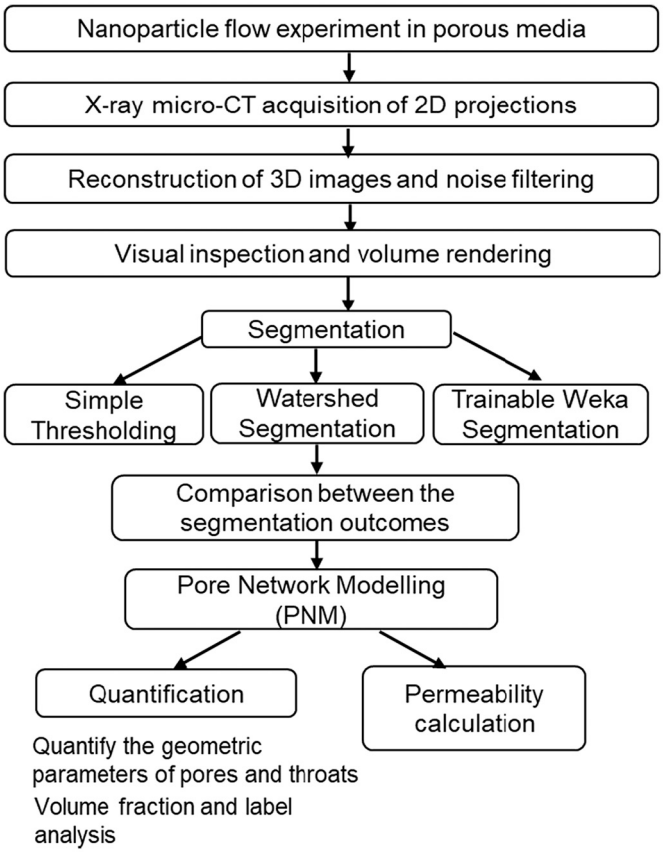

Fig. 3. The flow chart of image processing and analysis performed in this study.

2.2. Segmentation

Image segmentation involves the process of assigning, identifying, and isolating pixels (or voxels) in an image with labels sharing similar characteristic (Martínez-Martínez et al., 2007). Image segmentation enables the different phases (i.e., pores, sand grains, and nZVI) within the image to be identified. The literature reports several segmentation techniques; however, none is known to provide a solution for all images (Kaestner et al., 2008). Therefore, a successful segmentation is achieved through application of several different techniques and comparison of the results against what is expected or known from the sample. Here image segmentation allowed the identification of the pores, grains, and nZVI phases within the volumes under study. The simplest segmentation technique, i.e., thresholding worked reasonably well for some of the images and phases (SI Appendix, Fig. S1 and Fig. S2). Other phases (nZVI) needed more advanced segmentation. For this trainable Weka segmentation algorithm implemented in ImageJ and watershed segmentation in Avizo were used.

2.2.1. Trainable Weka segmentation (TWS)

The Trainable Weka segmentation (TWS) is a machine learning tool implemented in ImageJ (Arganda-Carreras et al., 2017). Here the TWS was used particularly to segment the nZVI phase. The segmentation was successful for all the phases using the TWS technique. Fig. 4 shows the outcome of TWS for the four samples studied in this work.

The segmented images of each phase were then studied using the label analysis algorithms within Avizo (particle analyser in ImageJ offers a similar possibility). Label analysis identifies the individual objects within each phase, each object is a connected cluster of voxels (Dillencourt et al., 1992). Labelling was used to identify and quantitatively analyse connected objects in each image. This included measurement of their shape, size, elongation, specific surface area, porosity, and saturation of each phase etc. 3D image visualisation (volume rendering of phases) was performed in Avizo.

2.3. Pore network model extraction

In this study, the objective of extracting PNMs is to (i) carry out numerical simulation of fluid flow (single phase) on the segmented pore space (connected part), and (ii) quantify the geometric parameters of the network elements (pores and pore throats) before and after nZVI injection.

To extract PNMs the first step is to generate the skeleton of the pore space (one-voxel thick) that shows how the network is connected. This skeleton is produced using a thinning process by eroding the pore phase starting from the pore-grain interface. This is also known as skeletonization which involves calculating the shortest distance between the void space and the background (Fouard et al., 2004). Using the skeleton, the pore space can be separated into pores and pore throats. Here, the pores are spherical in shape, the pore throats are straight cylindrical channels. Pore space connectivity is measured through a parameter known as coordination number. The unconnected pore space consists of isolated cluster of pores that in fact may be connected to the pore system but through pore-throats smaller than the image resolution and hence appear as disconnected. This is a known limitation of imaging techniques such as the one used in this work. There is a trade-off between the sample size and the image resolution meaning that a better image resolution is achievable for smaller samples. At the time of writing this paper, with the existing X-ray μCT imaging instruments, image resolution of a few μm is achieved for samples of a few mm size. See the following review paper for a more comprehensive discussion on X-ray μCT imaging limitations (Wildenschild and Sheppard, 2013). While a few μm resolution is sufficient to resolve pore-space clogging and its impact on flow properties (such as permeability of the porous media), the individual nanoparticles are not resolved using these images. Therefore, a pore-by-pore study of nanoparticle movements through the pore space in 3D is not yet possible. Additionally, potential deposition of nanoparticles on the sand grain surfaces can go undetected unless they form layers with thicknesses approaching the image resolution. This limitation can potentially be overcome through investigating sand grains using SEM or TEM after the μCT imaging is done and the column is taken apart. This, however, is a destructive technique which will only

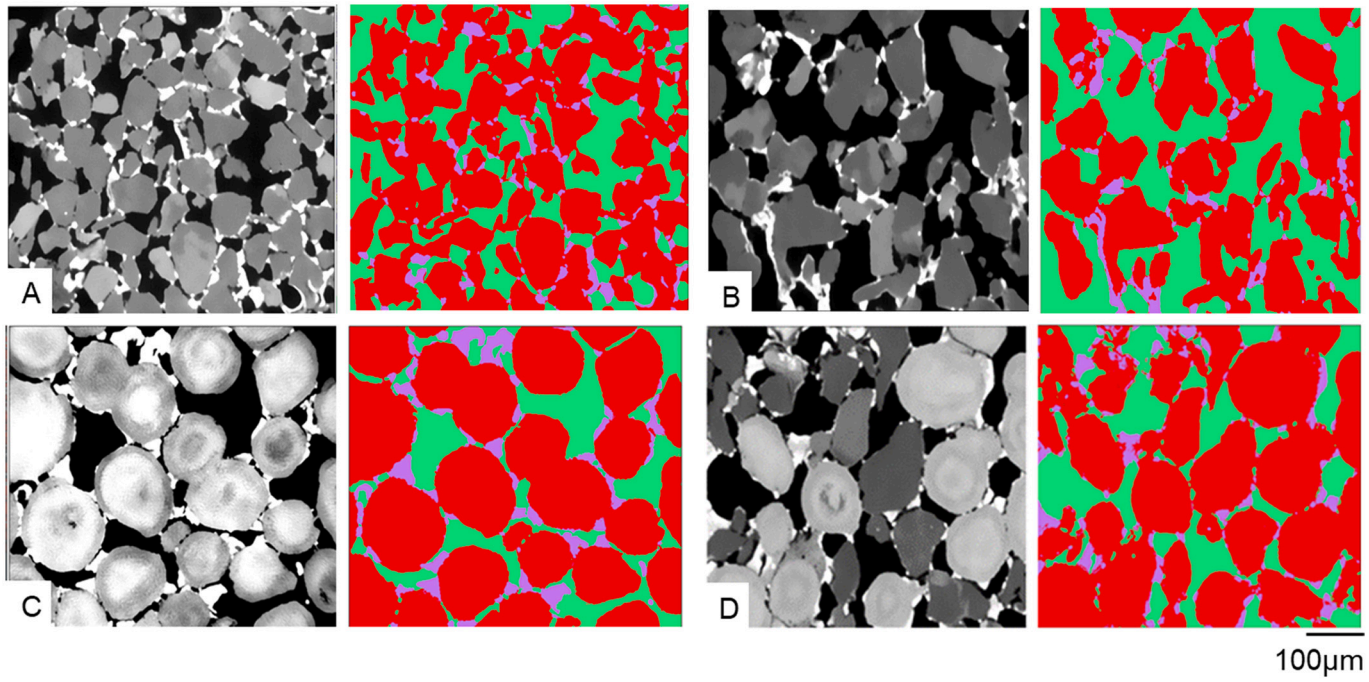

Fig. 4. TWS results showing grains (red); pores (green); NP (purple) for fine sand (A); coarse sand (B); carbonate (C) and mixed sample (D). (For interpretation of the references to colour in this figure legend, the reader is referred to the web version of this article.)

Table 1
Dimensions of the four 3D images used in this study.

Column	Image dimensions x, y, z (voxels)	Image dimensions x, y, z (μm)	Image size (MB)
Fine sand	988× 1011 × 892	600× 600 × 600	464.1
Coarse sand	988× 1011 × 942	600× 600 × 600	334
Mixed sand	988× 1011 × 993	600× 600 × 600	366.5
Carbonate	988× 1011× 998	600× 600 × 600	363.9

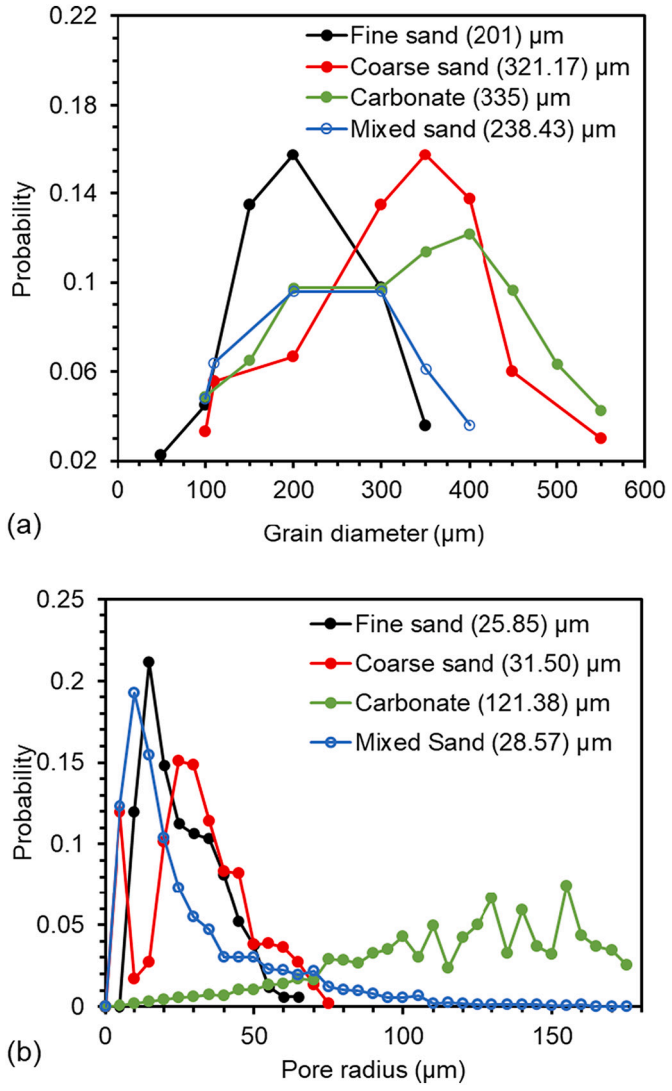

Fig. 5. (a) Grain size distribution for all the samples, (b) Pore size distribution of the four samples under study.

be useful to confirm nZVI deposition on the grains without considering the pore system they were forming in the sand column.

The absolute permeability of the rock is calculated based on the segmented pore phase (connected portion) using the PNM module in Avizo. Table 1 shows the dimensions of the images used in this study.

3. Result and discussion

In this section we present and discuss the PNMs extracted from the four columns under study. We compare their characteristics including shape factor, size distribution, and coordination number. We also present the porosity, permeability, and tortuosity data extracted from the

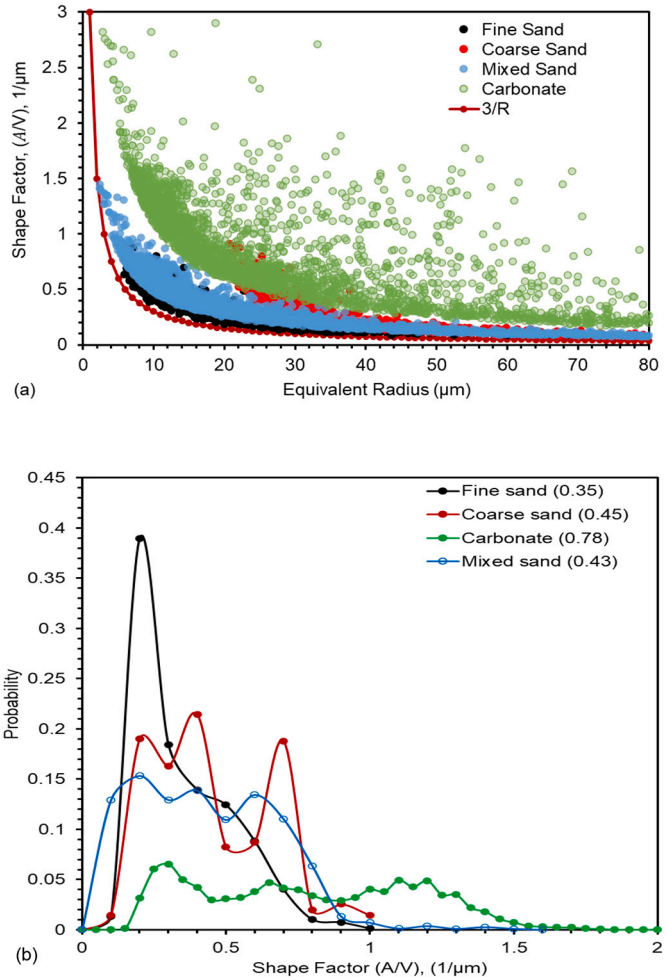

Fig. 6. (a) Pore shape factor against Equivalent radius of the four samples, (b) Pore shape factor distribution (histogram) in the four samples.

images under study. For the presented distributions the mean value is shown in brackets.

3.1. Grain and pore size distributions

The grain size distributions for the samples under study are presented in Fig. 5a. The coarse sand displays grains with a larger size (peak grain size of 321 μm) compared to the fine sand (peak grain size of 201 μm). Both the coarse and carbonate sand columns have grain sizes ranging between 100 μm to 550 μm. The mixed sample presents grain sizes ranging from 100 μm to 400 μm. The fine and mixed samples have narrow grain size distributions.

The difference in grain size (and therefore pore size) distributions is reflected in the difference in the porosity for these samples. Fine, coarse, carbonate, and mixed sand columns have porosities of 33, 39, 49 and 35%, respectively. Having the highest porosity, as shown in Fig. 5b, the carbonate sample also has the largest average pore radius of 121.38 μm. In contrast, fine sand displays the lowest porosity as well as the smallest average pore radius of 25.85 μm. The fine sand, mixed sand and the carbonate have a unimodal pore size distribution with a long tail towards larger pore sizes. Coarse sand has a bimodal distribution with the location of their peaks at slightly higher pore sizes. The average pore radius of coarse sand and mixed sand samples are between 31.50 μm and 28.57 μm.

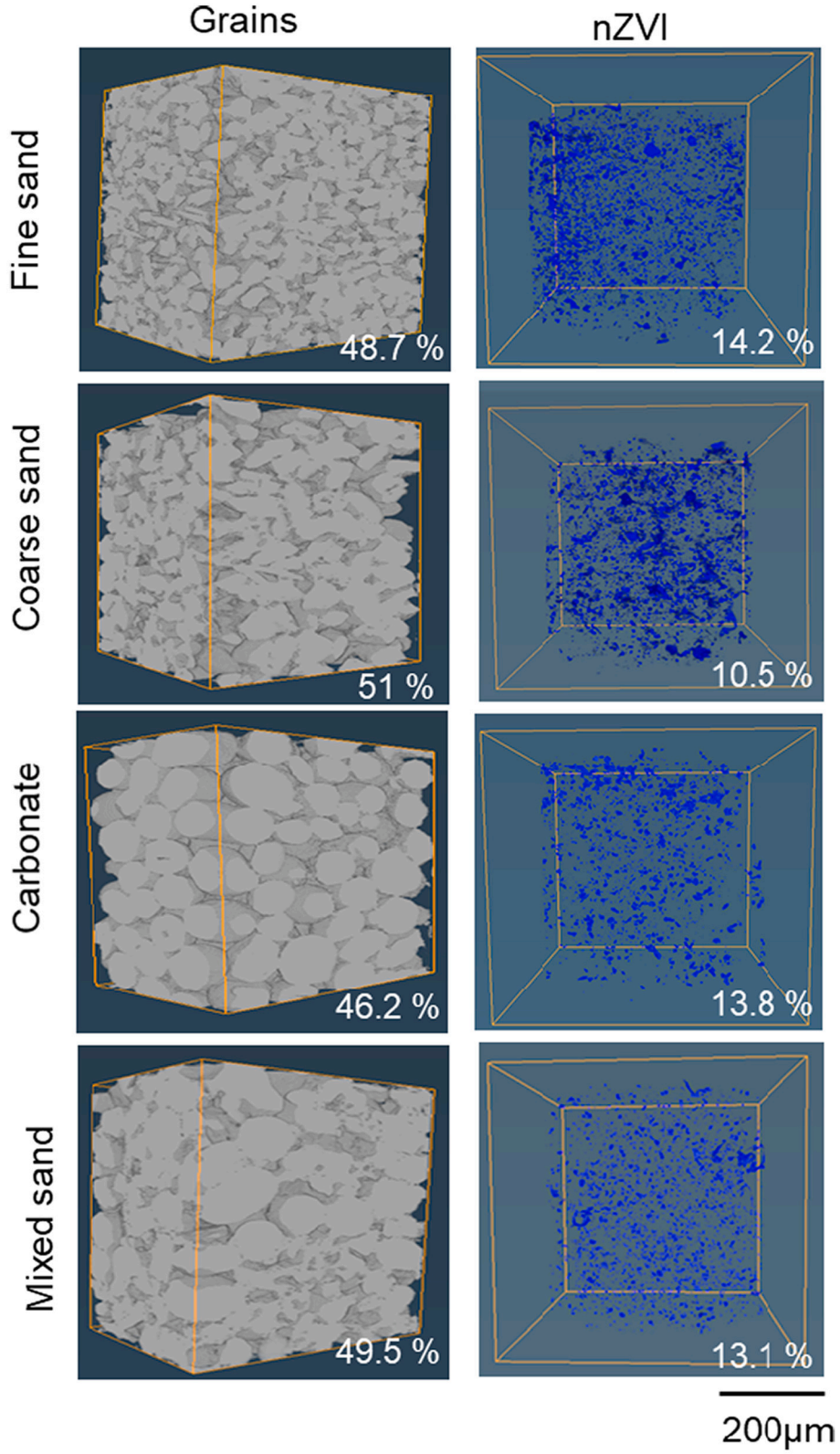

Fig. 7. 3D renderings of the grains (left) and the retained nZVI phase (right). The percentage of each phase is shown in the bottom right. The pore phase is shown in (SI Appendix Fig. S4).

3.2. Specific surface area (SSA)

SSA is the surface that is available per volume of sand for nZVI to attach defined as $(\frac{A_g}{V_g})$, where A_g is the surface area of sand, (μm^2) and V_g is the volume of sand, (μm^3). SSA is 5.78, 5.59, 10.67, 8.35 μm^{-1} for fine sand, coarse sand, carbonate, and mixed sand, respectively. Fine and coarse sand have similar SSA whereas the mixed sand is larger due to the presence of heterogeneous grains.

Table 2
Phase quantification for the four columns under study.

Rock type	Grains (%)	Pores (%)	nZVI (%)	nZVI saturation in the pore space (%)
Fine sand	48.7	37.1	14.2	38.3
Coarse sand	51	38.5	10.5	27.3
Carbonate	46.2	40	13.8	25.65
Mix sand	49.5	37.4	13.1	35.0

3.3. Pore shape

The pore shapes within the carbonate sample are distinctly different from the pores within the fine and coarse sand columns. The sand particles are angular while the carbonate grains are rounded objects. Angular grains can fit together more closely resulting in a better packed sample. The carbonate grains used here were obtained from the Ketton limestone which is an oolitic limestone from the UK. As shown in Fig. 4 the grains (voids) form close to spherical shapes. As a result, the intergranular pores formed in the carbonate column takes a close to star shape. Analysis of the images show that the column packed with the carbonate grains presents the largest surface per volume. This is an important parameter for nZVI particle attachment and retention.

In PNM studies the pore shape is commonly evaluated using a parameter known as the shape factor which is defined as $G = \frac{A}{V}$ (An et al., 2016), where A is the pore area (μm^2), V is the pore volume (μm^3). The pore shape factor distribution for the four columns under study is presented in Fig. 6a. As expected, this Figure shows the carbonate column has highest G values while the fine sand shows the smallest G values. The plot also shows G for perfect spheres of radius R in the red curve. $G = \frac{3}{R}$ for spheres. Majority of the pores are irregular in shape as expected for real porous media (von Bargen and Waff, 1986). The distribution of the pore shape factors for the four different samples is shown in the Fig. 6b.

Deviation from spherical shape ($G \neq 1$) suggests pores are angular. Angular pores provide a more suitable environment for entrapment of nZVI clusters compared to spherical pores. The average pore shape factor is highest in carbonate 0.78 1/μm and lowest in fine sand 0.35 1/μm. The carbonate also shows a wider range of pore shape factors. While we show the pores and pore throats are angular using the real images, it should be noted that for simplicity we use a PNM approach that extracts spherical pores and cylindrical pore throats.

3.4. Analysis of saturation values of the different phases and volume rendering

Visual inspection using 3D renderings of the different samples and quantitative analysis provides an excellent means to understand the nZVI retention within the samples and allows phase quantification. Fig. 7 shows the 3D rendering for the grains and nZVI phases. Table 2 presents the percentage of each column occupied by the grains, pores, and nZVI phases after NP injection. As seen the nZVI saturation in the pore space (%) shows the highest amount in the column packed with the fine sand (38.3%). There is >10% difference between the amount of entrapped nZVI in the fine and coarse sand columns. This shows the significant impact of the pore-size distribution on particle trapping.

Carbonate sample has trapped the least amount of nZVI (25.65%) and agrees with its larger grain size and pore size. There are two main differences between the sand and the carbonate grains used in this study (i) mineralogy of the grains, (ii) grain shape and angularity. The former has direct impact on the surface charge of the grains (zeta potential) and can contribute to particle/solid interactions. The latter can impact the mechanical filtration of particles through creation of angular pore systems with pore corners and constricted spaces promoting particle entrapment.

3.5. Pore network modelling (PNM)

Through extracting pore networks, we studied key morphological parameters of the different porous media (the pore size distribution, pore throat size distribution, and individual pore geometries). These parameters are important for revealing the nZVI transport properties in the pore space of the different samples. 3D representation of the pore

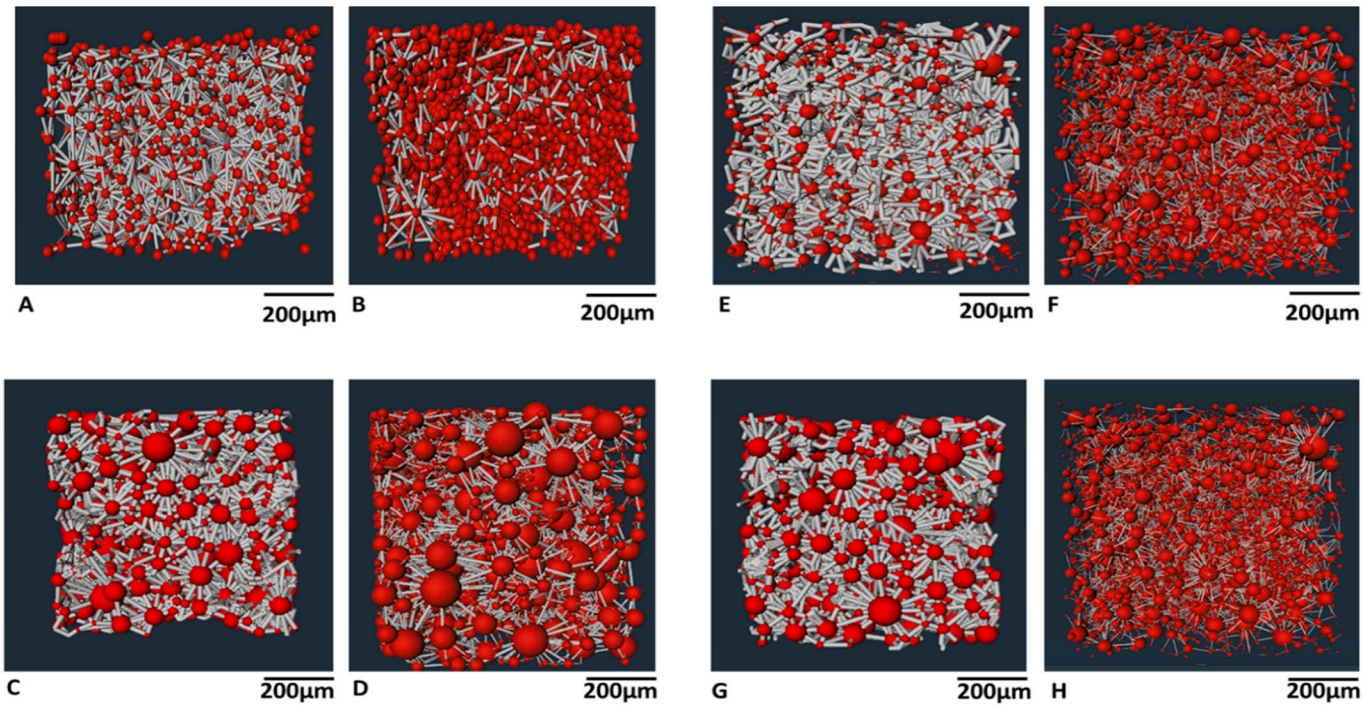

Fig. 8. PNMs extracted from the images before (A-D) and after (E-H) nZVI injection (fine sand A and E; coarse sand B and F; carbonate C and G and mixed sand D and H).

Table 3
Topologic parameters of the pore network before and after nZVI injection. The brackets show the statistical results of the pore network after nZVI injection.

Sample	Fine sand	Coarse sand	Carbonate	Mixed sand
Number of pores	1516 (2283)	1538 (2366)	1481 (3813)	1603 (3620)
Number of pore throats	8828 (9726)	8191 (8613)	7820 (9354)	8403 (9080)
Average radius of pores (μm)	25.85 (10.74)	31. 50 (21.06)	121. 38 (38.46)	28.57 (19.93)
Average radius of throats (μm)	11.56 (6.83)	18.36 (11.56)	23.09 (17.63)	14.25 (10.83)
Average coordination number	7.34 (4.12)	7.41 (4.80)	7. 60 (2.24)	6.57 (2.21)

network model extracted from the four samples are shown in Fig. 8 above. The pore space is illustrated as a lattice of pores (shown as spheres) connected by pore throats (shown as cylinders). The size of pore or pore throat indicates the inscribed radius.

Table 3 presents the quantitative analysis of these PNMs. The mixed sand has the highest number of pores (1603), and carbonate has the smallest pore count (1481). The table also reports the statistics for the PNM generated for the pore phase after the nZVI injection. Pores and throat counts increase after nZVI injection in all the samples. This is because nZVI deposition has altered the pore space in a way that some pores or pore throats are split in more than one pore or pore throat with smaller sizes (Fig. 4). The analysis also shows a reduction in the pore sizes and pore throat sizes (Figs. 9 and 10 (b-e). This alteration affects the structure and the pore geometries. The significant increase in the number of pores and throats shows the marked change in the pore system for these columns as a result of nZVI injection.

The pore topology refers to the way the pores are interconnected. Pore topology parameters such as the coordination number were studied. As can be seen from Table 3, carbonate sample has the smallest pore and throat count but has a slightly higher coordination number compared to the other samples.

3.5.1. Pore size distribution

Studying pore size distributions provides valuable insights into the structure of porous media. Fig. 9 shows the effect of nZVI injection on the pore size distribution for the four samples studied. Pore size distributions are shown to be impacted by the NP injection in all samples. The analysis shows a slight shift in the size distribution towards the left (smaller sizes) after nZVI injection. If we consider the average pore size for the presented distributions the reduction rate is ~59% in fine sand, ~34% in coarse sand, ~70% in carbonate, and ~31% in mixed sand. The carbonate sample shows the highest reduction as some of the larger pores within this sample are either split in several pores or are completely clogged because of nZVI injection.

3.5.2. Pore throat size distribution

The pore throats serve as the connection between the pores and plays a vital role in the connectivity of the porous media. Pore throats are the narrows parts of the network that restrict the flow and can give rise to particle entrapment. Here quantitative analysis of the pore throat geometry before and after the nZVI injection is presented. Fig. 10a shows the pore throat size distribution and Fig. 10(b-e) shows the effect of nZVI injection on the pore throat size in the samples studied.

The pore throat sizes display a unimodal distribution for all samples with a long tail towards larger throat sizes. The mean pore throat radius of carbonate (23.09 μm) is the largest and the mean for the fine sand (11.56 μm) is the smallest. The coarse and the mixed porous sand display mean pore throat size of 18.36 μm and 14.25 μm, respectively. nZVI injection has resulted in reduction of the pore throat sizes leading to the pore throat distributions moving to the left. The reduction in the average throat sizes range from ~24% to~ 41% due to closure of the larger throats (41% in fine sand, 38% in coarse sand, 25% in carbonate and 24% in mixed sand).

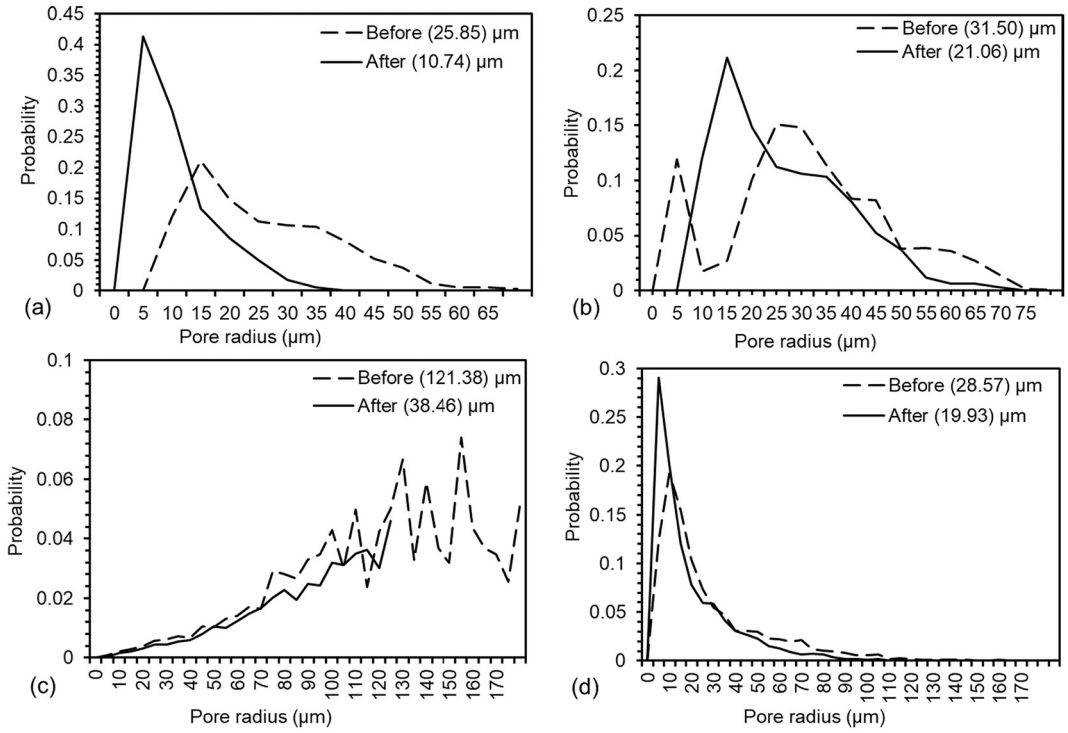

Fig. 9. Pore radius distribution before and after nZVI injection for fine sand (a), coarse sand (b), carbonate (c), and the mixed sample (d).

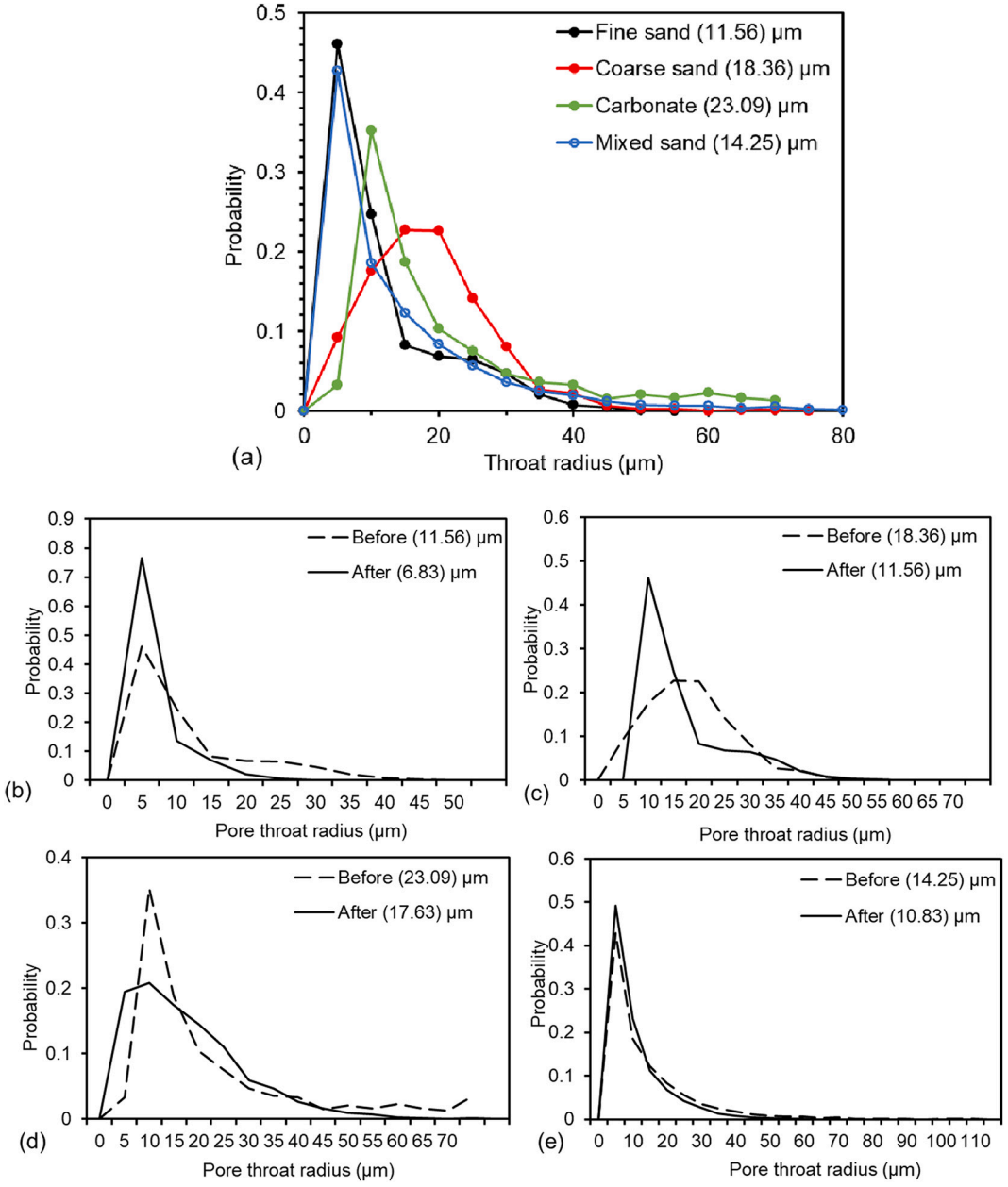

Fig. 10. (a) Pore throat size distribution for the samples studied, (b-e) Pore throat radius distribution before and after nZVI injection. Fine sand (b), coarse sand (c), carbonate (d), and the mixed sample (e).

3.5.3. *Throat channel length distribution*

Figure 11a below presents the throat channel length distribution and Fig. 11b shows the effect of nZVI injection on the throat channel length. This describes the trapping mechanism by telling us about the longest path within the sample through which the nZVI will pass. The throat channel length distribution in fine sand, coarse sand and mixed sand shows a unimodal distribution, and their distribution is nearly symmetric. Carbonate shows a bimodal distribution with a larger average throat channel length distribution of 92.91 μm. Fine sand has an average throat channel length distribution of 47.92 μm with the largest peak at reduced throat channel length. Coarse sand (84.57) μm and mixed sand (82.85) μm has similar average throat channel length distribution. The peak of the mixed sand is slightly higher than that of coarse sand at the throat channel length range around 70 μm to 80 μm. Fig. 11b shows the effect of nZVI injection on all the samples. The throat channel length is seen to be moving towards the left in all the samples after nZVI injection. Also, the peak of the throat channel length moves towards reduced throat channel length with a higher probability in fine, coarse, and mixed sand.

3.5.4. *Coordination number distribution*

The coordination number has proven to impact transport properties (Liu et al., 2022). Fig. 12a bellow shows the coordination number distribution for all the samples. The effect of nZVI injection on the coordination number is shown in Fig. 12(b-e). Fig. 12a shows that the coordination number distribution in all the samples follows a unimodal distribution with the tail towards larger coordination number. Fig. 12a shows that the fine sand has the best connectivity with the highest average coordination number of 10. Coarse sand, carbonate and mixed sand have similar coordination number of 6.82, 6.15 and 5.62 respectively. The better connectivity in fine sand provides more pathways to flow. Fig. 12b shows that nZVI injection has reduced the coordination number in all samples. Fine sand shows a reduction of approximately 44%, coarse sand 36%, carbonate 71%, and mixed sand 63%,

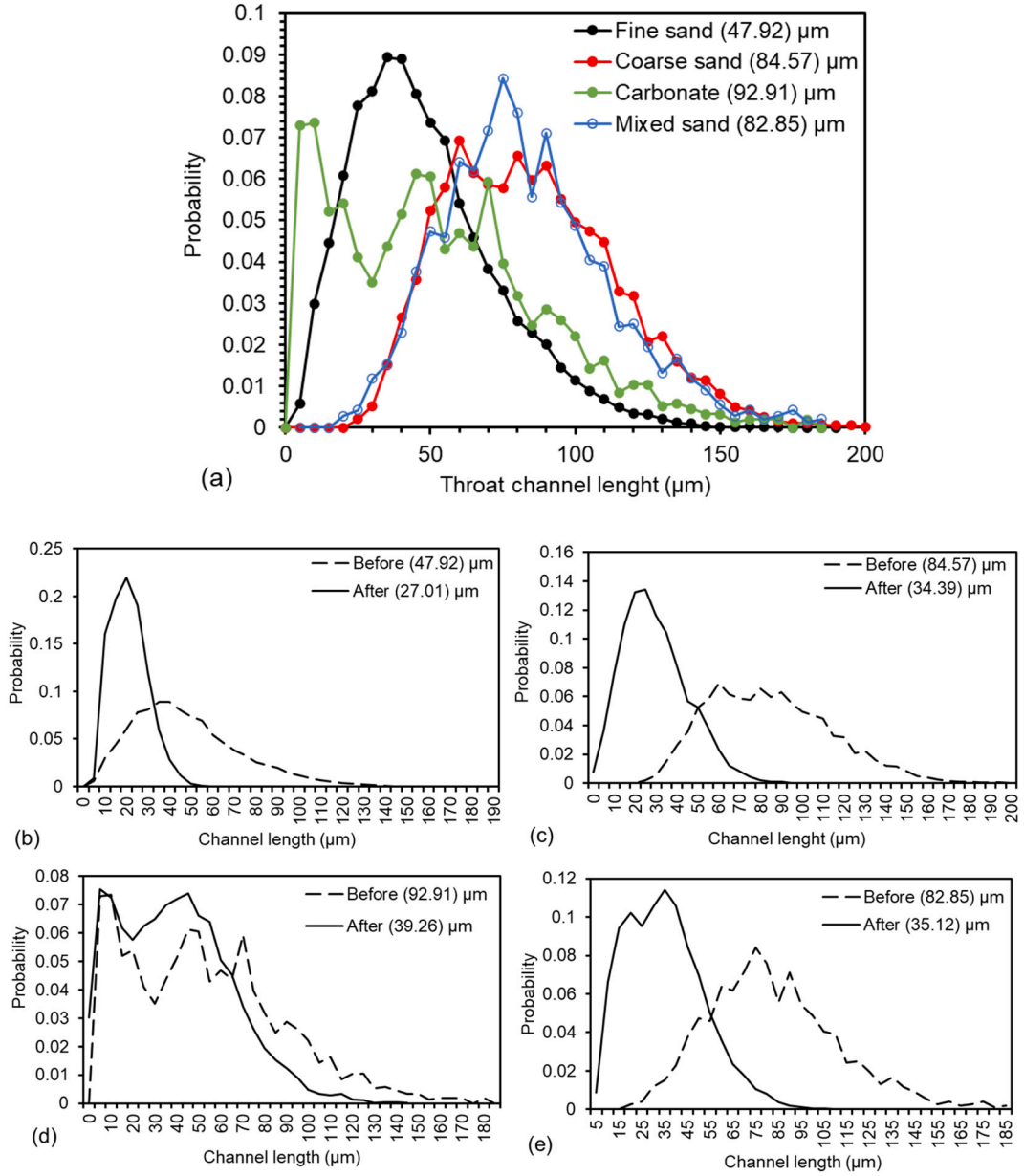

Fig. 11. (a) Pore throat channel length distribution for the samples studied, (b) pore throat channel length distribution before and after nZVI injection.

respectively, compared to their initial coordination numbers. The nZVI injection has created a great number of isolated pores in carbonate and mixed sand.

3.6. Evaluation of flow properties

Our analysis shows that permeability reduces as a result of the nZVI injection in the four columns under study (see Table 4). Carbonate has the highest initial permeability due to its larger pore throat sizes. The carbonate has fewer pore throats (7820) which are longer and wider. It is noted that the PNMs display a similar pore counts for all four samples. Permeability reduction is highest for the fine sand (98.94) % and smallest in coarse sand (73.89) %. This reduction is also seen with the highest reduction of its pore throat radius of 41% in fine sand. This shows the importance of the pore throat radius on the permeability of the porous media. Permeability reduction is more pronounced in fine sand sample with its smaller grain sizes. The fine sample has retained the highest amount of nZVI. Although we observe a difference in permeability reduction for all the samples, the porosity reduction was similar for all the tested porous media. The nZVI injection does not cause a significant change in tortuosity. Reduction in porosity and permeability with increase in tortuosity changes the pore geometry.

This shows that there are fewer junctions in the large conduits of the carbonate sample. This analysis shows that the fine sand has short and narrow throats joining its pores. It is seen that the larger pores are connected to more throats and the longer throats have a wider distribution in all the samples (SI Appendix, Fig. S3).

4. Summary and conclusions

This paper presents a pore-scale imaging study aiming to quantitatively analyse the mobility and retention of nZVI nanoparticles within columns packed with grains of different sizes and compositions. We use X-ray μ-CT imaging to study the nZVI distribution within these four columns before and after the injection of nZVI, non-destructively. We present the outcome of our analysis focusing on the flow properties (porosity and permeability) as well as geometrical and topological pore-scale properties (pore geometry and connectivity). Our 3D images show

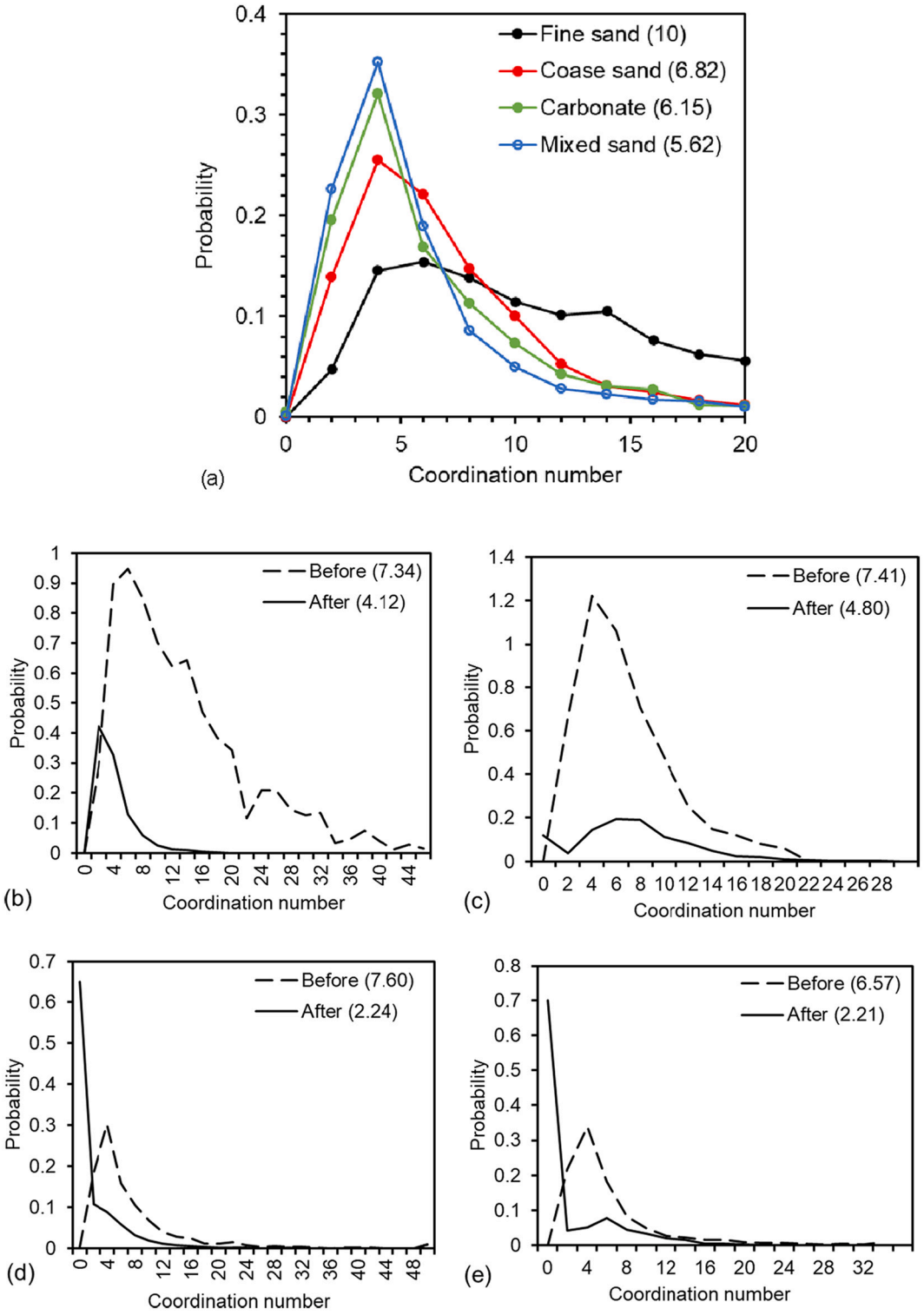

Fig. 12. (a) Coordination number distribution in all the samples (for comparison purposes, values ≤20 is shown), (b-e) Effect of nZVI injection on the coordination number.

the extent and nature of the pore space clogging due to nZVI deposition and its effects on the pore size, pore throat size, pore throat length and coordination number. We conclude that nZVI transport in porous media is impacted by the mineral composition of the grains as well as the size and geometry of the pore space. The following conclusions can be extracted from this study:

- Pore-scale imaging using X-ray μ-CT can be successfully applied to study nZVI mobility and entrapment in sandy porous media. This study highlights the suitability of μCT imaging for visualising and quantification of nZVI clogging at the pore-scale.
- Analysis of X-ray μCT images allowed to gain insight into the effect of grain composition and size on the transport of NP.

Table 4
Transport properties before and after nanoparticle injection.

Sample ID	Porosity before	Porosity after	% Porosity reduction	Permeability before (D)	Permeability after (D)	% Permeability reduction	Tortuosity before	Tortuosity after	% Tortuosity increase
Fine sand	0.33	0.21	36.36	5.67	0.06	98.94	2.18	2.27	4.13
Coarse sand	0.39	0.25	35.90	9.27	2.42	73.89	1.85	1.86	0.54
Carbonate	0.49	0.31	36.73	10.23	0.82	91.98	1.84	1.86	1.09
Mixed sand	0.35	0.22	37.14	6.44	0.58	90.99	1.72	1.75	1.74

- The amount and distribution of nZVI deposited controls the permeability loss in porous media. The measured porosity and permeability reduce significantly in all the columns.
- Although the carbonate has a larger surface area (per unit volume of pores) available for nZVI attachment, this has not resulted in an increase in the total nZVI retention within the carbonate column. This suggests that nZVI retention is predominantly contorted by pore structure rather than the mineralogy of the grains.
- All the pore scale geometrical and topological properties studied here (i.e., pore and pore throat sizes, pore throat length, coordination number) are shown to be significantly reduced by the nZVI retention within the columns under study.
- The column porosity reduces in the range of ~35% to ~37%, while permeabilities reduce in the range of ~73% to ~99%. The permeability reduction is more significant for the fine sand (~99%) compared to the coarse sand (~74%). In contrast, tortuosity does not show a significant increase (~1% to ~4%). Fine sand has entrapped the highest number of NPs (38%).
- Future work should focus on performing 4D (3D + time) experiments in which a sequence of images is captured during the nZVI injection in porous media. A similar study to the work published by Pak et al. (2020) which uses 4D imaging to study the use of nZVI for in-situ degradation of trichloroethylene.

Authorship contribution

Category 1. Conception and design of the study: Tannaz Pak; Nathaly Lopes Archilha

Aquisition of data. Raoul Djou Fopa; Anderson Camargo Moreira

Analysis and or interpretation of data: Raoul Djou Fopa; Tannaz Pak

Category 2. Drafting the manuscript: Raoul Djou Fopa

Revising the manuscript critically for important intellectual content: Raoul Djou Fopa; Carlo Bianco; Tannaz Pak; Nathaly Lopes Archilha; Anderson Camargo Moreira

Category 3. Approval of the version of the manuscipt to be published: Raoul Djou Fopa; Carlo Bianco; Tannaz Pak, Nathaly Lopes Archilha; Anderson Camargo Moreira

Declaration of Competing Interest

The authors declare that they have no known competing financial interests or personal relationships that could have appeared to influence the work reported in this paper.

Data availability

Data will be made available on request.

Acknowledgement

We are grateful for financial support from the São Paulo Research Foundation (FAPESP) (Grant 17/20308-0) and Teesside University (Grand Challenges Seed Fund). We appreciate the outstanding support of the LNLS staff, especially the chemistry laboratory and the user office.

Appendix A. Supplementary data

Supplementary data to this article can be found online at https://doi.org/10.1016/j.jconhyd.2022.104126.

References

Al-Raoush, R.I., Willson, C.S., 2005. A pore-scale investigation of a multiphase porous media system. J. Contam. Hydrol. 77 (1), 67–89.
An, S., et al., 2016. Influence of pore structure parameters on flow characteristics based on a digital rock and the pore network model. J. Nat. Gas Sci. Eng. 31, 156–163.
Arganda-Carreras, I., et al., 2017. Trainable Weka segmentation: a machine learning tool for microscopy pixel classification. Bioinformatics 33 (15), 2424–2426.
von Bargen, N., Waff, H.S., 1986. Permeabilities, interfacial areas and curvatures of partially molten systems: results of numerical computations of equilibrium microstructures. J. Geophys. Res. Solid Earth 91 (B9), 9261–9276.
Baychev, T.G., Jivkov, A.P., Rabbani, A., Raeini, A.Q., Xiong, Q., Lowe, T., Withers, P.J., 2019. Reliability of algorithms interpreting topological and geometric properties of porous media for pore network modelling. Transp. Porous Media 128 (1), 271–301.
Beryani, A., et al., 2020. Key factors affecting graphene oxide transport in saturated porous media. Sci. Total Environ. 698, 134224.
Bianco, C., et al., 2017. Controlled deposition of particles in porous media for effective aquifer nanoremediation. Sci. Rep. 7 (1), 1–10.
Buades, A., Coll, B., Morel, J., 2005. A non-local Algorithm for Image Denoising. Paper Presented at the 2005 IEEE Computer Society Conference on Computer Vision and Pattern Recognition (CVPR'05), 2 60–65.
Chen, Z., et al., 2015. Microstructural characteristics and elastic modulus of porous solids. Acta Mater. 89, 268–277.
Dillencourt, M.B., Samet, H., Tamminen, M., 1992. A general approach to connected-component labeling for arbitrary image representations. J. ACM (JACM) 39 (2), 253–280.
Dordzie, G., Dejam, M., 2021. Enhanced oil recovery from fractured carbonate reservoirs using nanoparticles with low salinity water and surfactant: a review on experimental and simulation studies. Adv. Colloid Interf. Sci. 293, 102449.
Fouard, C., et al., 2004. Skeletonization by blocks for large 3D datasets: Application to brain microcirculation. In: 2004 2nd IEEE International Symposium on Biomedical Imaging: Nano to Macro (IEEE Cat No. 04EX821). IEEE.
Hidajat, I., et al., 2002. Transport properties of porous media reconstructed from thin-sections. SPE J. (Soc. Petrol. Eng. (U.S.): 1996) 7 (1), 40–48.
Kaestner, A., Lehmann, E., Stampanoni, M., 2008. Imaging and image processing in porous media research. Adv. Water Resour. 31 (9), 1174–1187.
Karn, B., Kuiken, T., Otto, M., 2009. Nanotechnology and in situ remediation: a review of the benefits and potential risks. Environ. Health Perspect. 117 (12), 1813–1831.
Li, X., Elliott, D.W., Zhang, W., 2006. Zero-valent Iron nanoparticles for abatement of environmental pollutants: materials and engineering aspects. Crit. Rev. Solid State Mater. Sci. 31 (4), 111–122.
Lindquist, W.B., et al., 2000. Pore and throat size distributions measured from synchrotron X-ray tomographic images of Fontainebleau sandstones. J. Geophys. Res. Solid Earth 105 (B9), 21509–21527.
Liu, H., Ma, C., Zhu, C., 2022. X-ray Micro CT based characterization of pore-throat network for marine carbonates from South China Sea. Appl. Sci. 12 (5), 2611.
Madonna, C., et al., 2013. Synchrotron-based X-ray tomographic microscopy for rock physics investigations synchrotron-based rock images. Geophysics 78 (1), D53–D64.
Martínez-Martínez, J., Benavente, D., Del Cura, M.G., 2007. Petrographic quantification of brecciated rocks by image analysis. Application to the interpretation of elastic wave velocities. Eng. Geol. 90 (1–2), 41–54.
Mohammadian, S., Krok, B., Fritzsche, A., Bianco, C., Tosco, T., Cagigal, E., Mata, B., Gonzalez, V., Diez-Ortiz, M., Ramos, V., 2021. Field-scale demonstration of in situ immobilization of heavy metals by injecting iron oxide nanoparticle adsorption barriers in groundwater. J. Contam. Hydrol. 237, 103741.
Mondino, F., et al., 2020. Injection of zerovalent iron gels for aquifer nanoremediation: lab experiments and modeling. Water 12 (3), 826.
Olayiwola, S.O., Dejam, M., 2019. A comprehensive review on interaction of nanoparticles with low salinity water and surfactant for enhanced oil recovery in sandstone and carbonate reservoirs. Fuel 241, 1045–1057.
Pak, T., et al., 2016. Multiscale pore-network representation of heterogeneous carbonate rocks. Water Resour. Res. 52 (7), 5433–5441.
Pak, T., Archilha, N.L., Mantovani, I.F., Moreira, A.C., Butler, I.B., 2018. The dynamics of nanoparticle-enhanced fluid displacement in porous media-a pore-scale study. Sci. Rep. 8 (1), 1–10.

Pak, T., Archilha, N.L., Luz, Lima, Fernando, Luiz, de., 2019. Nanotechnology-based remediation of groundwater. Nanotechnology characterization tools for environment, health. In: and safety. Springer, pp. 145–165.
Pak, T., Jr, Luz, Fernando, Luiz, de Lima, Tosco, Costa, G.S.R., Rosa, P.R.R., Archilha, N. L., 2020. Pore-scale investigation of the use of reactive nanoparticles for in situ remediation of contaminated groundwater source. Proc. Natl. Acad. Sci. 117 (24), 13366–13373.
Raoof, A., Hassanizadeh, S.M., Leijnse, A., 2010. Upscaling transport of adsorbing solutes in porous media: Pore-network modeling. In: First International Conference on Frontiers in Shallow Subsurface Technology. European Association of Geoscientists & Engineers.
Ryazanov, A.V., Dijke, Van, Jan, Marinus Izaak, Sorbie, K.S., 2009. Two-phase pore-network modelling: existence of oil layers during water invasion. Transp. Porous Media 80 (1), 79–99.
Sanematsu, P.C., Thompson, K.E., Willson, C.S., 2019. Pore-scale modeling of nanoparticle transport and retention in real porous materials. Comput. Geosci. 127, 65–74.
Schiefler, A.A., Bruns, S., Müter, D., Uesugi, K., Sørensen, H.O., Tobler, D.J., 2022. Retention of sulfidated nZVI (S-nZVI) in porous media visualized by X-ray μ-CT–the relevance of pore space geometry. Environ. Sci.: Nano 9 (9), 3439–3455.
Seetha, N., et al., 2017. Upscaling of nanoparticle transport in porous media under unfavorable conditions: pore scale to Darcy scale. J. Contam. Hydrol. 200, 1–14.
Sharqawy, M.H., 2016. Construction of pore network models for Berea and Fontainebleau sandstones using non-linear programing and optimization techniques. Adv. Water Resour. 98, 198–210.
Suryanarayana, C., Mukhopadhyay, D., Patankar, S.N., Froes, F.H., 1992. Grain size effects in nanocrystalline materials. J. Mater. Res. 7 (8), 2114–2118.
Tiraferri, A., et al., 2017. Colloidal behavior of goethite nanoparticles modified with humic acid and implications for aquifer reclamation. J. Nanopart. Res. 19 (3), 1–11.
Wildenschild, D., Sheppard, A.P., 2013. X-ray imaging and analysis techniques for quantifying pore-scale structure and processes in subsurface porous medium systems. Adv. Water Resour. 51, 217–246.
Wu, K., et al., 2006. 3D stochastic modelling of heterogeneous porous media–applications to reservoir rocks. Transp. Porous Media 65 (3), 443–467.
Xiong, Q., Baychev, T.G., Jivkov, A.P., 2016. Review of pore network modelling of porous media: experimental characterisations, network constructions and applications to reactive transport. J. Contam. Hydrol. 192, 101–117.
Yu, H., Kotsmar, C., Yoon, K.Y., Ingram, D.R., Johnston, K.P., Bryant, S.L., Huh, C., 2010. Transport and Retention of Aqueous Dispersions of Paramagnetic Nanoparticles in Reservoir Rocks (Paper presented at the SPE Improved Oil Recovery Symposium).
Zhang, L., Chao, J., Geng, S., Zhao, Z., Chen, H., Luo, Y., Qin, G., 2020. Particle migration and blockage in geothermal reservoirs during water reinjection: laboratory experiment and reaction kinetic model. Energy 206, 118234.